Supporting Information

Ricicova et al. 10.1073/pnas.1215850110

SI Materials and Methods

Chip Fabrication. Microfluidic devices were fabricated from polydimethylsiloxane (PDMS; RTV-615, Momentive) by multilayer soft lithography (1, 2). The design of the chip as well as the fabrication procedure were described previously (3) except for the following differences. The chambers were fabricated using SU8-2 photoresist (Microchem) to achieve 2 μm in height. The dimensions of the chambers were 420 × 165 × 2 μm, and each chamber had eight pillars to prevent collapsing of the ceiling. We placed a 2-μm high fiduciary feature next to each chamber that served as a reference for autofocus during time-lapse microscopy. Two-layered chip was plasma bonded to a 0.21-mm Schott D263 borosilicate glass slide (SI Howard Glass) compatible with 63× objective.

Construction of the Strains. The list of yeast strains used in this study is in Table S1. All strains are mating type *MATa* and they were derived from the diploid strain BY4743 (S288C background). They are deleted for *BAR1* gene encoding pheromone protease and contain three fluorescent markers: Cdc10-YFP fusion protein that localizes in the budneck, PRE-mCherry reporter of pheromone pathway activity, and ACT1pr-yECFP reporter used for cell segmentation in the image analysis.

BAR1-HphNT1 cassette for *BAR1* deletion was amplified from pFA6a-hphNTI vector (4). Plasmid pKL973 carrying CDC10-YFP-LEU2 construct was kindly provided by K. Lee (National Institutes of Health, Bethesda, MD). PRE-mCherry-HIS3 cassette was amplified from PRE-mCherry vector, which was made by swapping GFP in PRE-GFP vector (5) by mCherry from pBS34 plasmid (Yeast Research Center) using PacI and AscI restriction sites. Vector for generation of ACT1pr-yECFP-CaURA3 cassette was constructed by cloning ACT1 promoter fragment (amplified from BY4741 genomic DNA ~600 bp upstream from ACT1 ORF) in PvuII-HindIII restriction sites of pKT174 plasmid (EUROSCARF) upstream of yECFP coding sequence (6).

Here, pKL973 plasmid, cassettes with fluorescent markers ACT1pr-yECFP-CaURA3 and PRE-mCherry-HIS3, and BAR1-HphNT1 deletion cassette were first separately transformed in BY4743 diploid strain and their proper integration in the genome was verified by PCR and/or by fluorescence microscopy. Confirmed clones were sporulated and haploid strains with individual markers were selected and consecutively crossed with each other to obtain a parental strain 737D with all three fluorescent markers and *BAR1* deletion. Additional knockouts of pheromone pathway genes were made by PCR gene replacement with kanMX deletion cassette amplified from pFA6a-GFP (S65T)-kanMX6 vector.

Growth Conditions. Yeast strains were cultured overnight in rich media at 30 °C and then diluted in fresh synthetic complete dextrose (SCD) media with 2% (wt/vol) glucose and grown to exponential phase. Cells were centrifuged at 1,957 × g for 2 min and concentrated in SCD supplemented with 0.2% BSA (Sigma Aldrich) to an $OD_{600} = 1$ up to 4 depending on the desired seeding density. Cells were then mixed 1:1 with a 3% (wt/vol) gel of low melting agarose (Sigma Aldrich) dissolved in SCD to reach final concentration of 0.1% BSA and 1.5% agarose. We have tested that 0.1% BSA still prevented α-factor from adhering to the walls of the PDMS channels/chambers and, unlike higher BSA concentrations, it did not affect growth rate of cells. The suspension was vortexed to homogeneity and transferred to the microfluidic device according to the protocol described previously (3). Before we opened diffusion valves that separate experimental chambers from feeding channels, all channels were primed with SCD supplemented with 0.5% BSA to further prevent adhering of chemicals to the PDMS walls. The 100n-M α-factor (ZymoResearch) and 250-mM hydroxyurea (Sigma Aldrich) were dissolved in SCD + 0.1% BSA. All solutions were stored in 2-mL custom-adapted vials (3), connected to the device by tubing, and pressurized by 2 psi air. Cells in the chip were grown at room temperature and divided approximately every 110 min compared with a doubling time of 125 min of a batch culture grown in the same conditions. This slightly faster growth in the chip may be due to frequent perfusion of fresh media as opposed to fixed media volume in tubes. Starting usually from 1 to 10 cells per chamber ($OD_{600} = 1$ before mixing with agarose gel) we ran experiments over 13 h before cells filled the chamber and began to stack on top of each other.

Image Acquisition and Chip Operation. The device was imaged using a Leica DMIRE2 inverted microscope and 63× oil immersion objective (HCX PL APO, NA 1.4–0.60). A Leica EL6000 light source with a high-speed shutter and mercury lamp (HXP R 120W/45C VIS, Osram) were used with three different filter cubes (Leica "YFP"; Leica "TX2"; Semrock "CFP-2432A-LSC-ZERO") for fluorescence imaging of YFP, mCherry, and CFP. To minimize photobleaching, the light source was operated at minimum intensity and the numerical aperture was maximized (N.A. 1.4) by fully opening the objective's iris. Bright-field images were captured through the YFP filter using a custom-installed light-emitting diode in place of the halogen lamp to enable quick switching between bright field and fluorescence. All images were captured with an ORCA-ER digital camera (Hamamatsu) capable of 1,344 × 1,024 pixel resolution. The microscope was fitted with a Prior Proscan III XY stage (1-mm ball screw, 50-nm encoders), enabling fast and precise scanning through the array of imaging chambers on the device, and was kept inside a rigid plastic enclosure to keep it isolated from ambient light and high-frequency fluctuations in room temperature.

Time-lapse imaging and perfusion of the array were controlled by a PC running LabVIEW 7.1 (National Instruments). To set up the experiment the user selected a subarray of chambers to be imaged, captured an image of a fiducial to be used as a template for pattern recognition, manually located and focused on three fiducials in the subarray, and calculated the x/y offset (constant across the array) between a chamber and its closest fiducial. The software then scanned through every fiducial in the subarray and captured a z-stack of bright-field images, using pattern recognition (IMAQ, National Instruments) to pinpoint the fiducial's exact *xy* location and autofocusing by selecting the image in the stack with the lowest variance. The *x*, *y*, and *z* coordinates of each fiducial were stored for future reference. At this point the user could select chambers to be imaged based on the quality of the autofocus and pattern-recognition results. Typically, over 98% of all chambers in the subarray were chosen for imaging. Finally, the user defined a time-dependent chemical condition for each row and the software began simultaneously perfusing and imaging the array.

Once imaging and perfusion began, the rest of the experiment was fully automated. Before each row was imaged for a given time point, the most recent chemical sent to the row was recorded for future reference. The imaging of a row began with the YFP filter, through which all bright-field and YFP images were acquired. At each fiducial in the row, autofocusing was performed to detect any change in z coordinate from the previous time point using a z stack of seven images at 0.5-μm spacing, following which the nearest chamber was imaged in bright field and YFP. The z coordinate of the chamber was inferred by interpolating or extrapolating stored z coordinates of nearby fiducials from the previous time point, and offsetting this by the change in height of the closest fiducial since the previous time point. Bright-field images (1× binning) were taken in focus as well as 3.5 microns above and below the focused position, and YFP images were taken in focus (2× binning, 200 ms exposure). After imaging of the entire row in YFP, imaging of the row was repeated (without autofocus) for CFP (2× binning, 100 ms exposure), and finally for mCherry (2× binning, 40 ms exposure), before moving on to the next row. Through the use of a high-speed shutter, the cells were only exposed to excitation light during fluorescent image capture so as to reduce photobleaching and exposure to potentially damaging high-frequency light. When imaging of the chip finished for a single time point, the stored fiducial z coordinates from the previous time point were replaced by the new ones and reimaging of the entire array began immediately.

Flat-Field Correction. Before any of the fluorescence images were used for analysis, the uneven illumination and collection efficiency of the microscope needed to be corrected. For each experiment, the user selected a single field of view and a time point to serve as a flat-field correction template for the entire experiment. The software used linear regression to fit a fourth-degree polynomial surface to the pixel intensities in the template image, ignoring regions in the image that the user identified as containing cells or high autofluorescence. By sampling this surface at the resolution of the fluorescence images and then dividing by the global maximum, a correction image was obtained. Three correction images were created, one for YFP, one for CFP, and one for mCherry, and these were used to correct every time point in every field of view for a given experiment.

It should be noted that all fluorescence images had and intensity of 197 (determined empirically) subtracted from them immediately after being read from disk to remove the effect of the camera's dark current.

Image Analysis Pipeline. To extract single-cell data and reconstruct lineages from thousands of cells we built a fully automated image-analysis pipeline in MATLAB (Mathworks). Flowchart of the image-analysis pipeline is shown in Fig. S14.

Cell segmentation. The two bright-field images (3.5 microns above and below the focus position) were normalized independently of each other so their pixel intensities occupied the entire range [0,1] (Fig. S15 *A* and *B*), and the difference between the two images was calculated. The diffraction patterns around the unfocused cells interfered constructively during this step, highlighting the cell boundaries while obscuring the background and cell bodies. The difference image was then renormalized (Fig. S15*C*) and thresholded using Otsu's method (7) to create a binary image, for which the number of black and white pixels was counted. If the image was more than 50% white pixels, an indication that many background pixels were incorrectly being considered part of the foreground, a second thresholding step was performed. All objects smaller than 50 pixels were removed from the thresholded images, which was then subjected to a morphological closing (structuring element: square with width 2) to remove small holes and smoothen edges, giving a binary image, B_{bnd}, that represented the cell boundaries (Fig. S15*D*).

Next, the normalized bright-field image from above the focus position (Fig. S15*A*) was used to make a mask of the cell colonies. The image was variance-filtered, renormalized to occupy the entire range [0,1] (Fig. S15*E*), thresholded using 0.5 times the threshold obtained from Otsu's method (this threshold was determined through iterative testing), and dilated (structuring element: disk with radius 7) (7). The background of the resulting image was identified as the collection of all objects in the complement image that were larger than 18,000 pixels, and all black pixels that were not part of the background were filled in. The image was then eroded (structuring element: disk with radius 7) to give B_{col}, a mask of the cell colonies (Fig. S15*F*).

Individual cells were identified using two methods. The first method removed the cell boundaries (B_{bnd}) from the cell-colony mask (B_{col}). This method occasionally missed small chunks when segmenting certain cells. The second method took the complement of B_{bnd} after using a flood-fill operation to fill in the background, producing false negatives in cases where the boundaries in B_{bnd} were not completely closed. By combining the results of these two methods using a pixelwise Boolean OR operator, a complete segmentation of all of the cells was created. A morphological opening (structuring element: square with width 3) was then used to eliminate small or thin objects, and touching cells were separated from each other using the watershed of the Euclidean distance function of the complement image. The h-maxima transformation was used to prevent oversegmentation. Objects smaller than 30 pixels or larger than 3,000 pixels were removed, as were objects that touched the edges of the image. This image, B_{bf}, still contained a few false positives (Fig. S15*G*).

To eliminate false positives, information from the CFP image was used. The pixel intensities in this image were first normalized to occupy the entire range [0,1] (Fig. S15*I*) and the image was then thresholded using Otsu's method (7). After a dilation of the resulting binary image (structuring element: square with width 5) the number of black and white pixels were counted and, if the dilated image was more than 75% white pixels, another thresholding step was performed on the undilated image. A morphological opening (structuring element: square with width 4) finished the segmented CFP image, B_{cfp} (Fig. S15*J*). Finally, the complement of B_{bf} was flood filled, using the white pixels in B_{cfp} as start locations, and the result was masked with B_{bf} (Fig. S15*H*). Any cell that touched the edge of the image was then removed, so that analysis was only performed on whole cells. In addition, cells within 200 pixels of the left edge (for the left field of view [FOV]) or 200 pixels from the right edge (for the right FOV) were assumed to be trapped under the chamber isolation valves and so were also removed from the segmented image.

Cell tracking. After the cell segmentation was complete for time point t, cells and lineages were tracked from time t-1 to time t. From previous iterations, each cell being tracked had already been assigned a label i. After assigning a temporary label j to each cell in time point t, the tracking problem was posed in terms of combinatorial optimization as the classic assignment problem, where the labels from t-1 acted as agents and the labels from t acted as tasks. The cost C_{ij} of assigning task j to agent i was taken to be $C_{ij} = D_{ij} + 0.25|S_j - S_i'|$ where D_{ij} was the Euclidean distance between the centroids of the two cells, S_j was this size of cell j, and S_i' was the estimated size of cell i after accounting for cell growth over the course of one time point. This size estimation was done by assuming that cells smaller than 75% of the median cell size will grow by 25% over one time point, while the rest of the cells remain the same size. The cost matrix C is then modified by giving infinite cost to the following elements: Elements with $D_{ij} > 25$; elements with $S_j/S_i' > 3$; elements with $S_j/S_i' < 0.66$; elements for which i is "full grown" and $S_j/S_i' > 1.25$; elements for which i is "full grown" and $S_j/S_i' < 0.8$; and elements for which label i has been retired. (A cell was considered to be "full-grown" if it was at least 25% larger than the median cell size.)

A version of the Hungarian algorithm (8) that was modified to work with rectangular weight matrices was used to solve the assignment problem given by the resulting cost matrix. From all of the assignments made by the algorithm, the median cost c_{med}

and mean absolute deviation of costs c_{mad} were calculated. Every task j that was unassigned by the algorithm was then assigned to the agent i, which gave the minimum cost if and only if (*i*) the cost satisfied $C_{ij} < c_{med} + 3c_{mad}$ and (*ii*) the agent i was not already assigned. All cells from time *t* that remained unassigned were assumed to be new cells and were given new labels. At this point, labels that had been unassigned for three consecutive time points (*t*, *t*-1, and *t*-2) were marked as "retired" and were avoided in future time points. The size of each cell and the location of its centroid were recorded for use in the next iteration of the tracking algorithm. For unassigned labels, the size and centroid location from the previous time point (*t*-1) were recorded instead.

Lineage tracking. Once cell tracking was completed for a given time point, information from the YFP image was used to perform lineage tracking. The pixel intensities in the YFP image were normalized to occupy the entire range [0,1], the budnecks were segmented using a local comparison and selection segmentation algorithm (9), and objects smaller than five pixels were removed.

For each segmented budneck, the two cells touching it were investigated to see if they formed a mother–daughter pair. If one cell was at least 1.5 times the size of the other, then the larger cell was proposed as the mother. Otherwise, no pairing was proposed from the given budneck. The overlap between the budneck and the proposed daughter was recorded as a measure of the confidence in the pairing. The proposed pairing was accepted and recorded only if the proposed daughter was not already identified as a mother, the proposed daughter appeared after the proposed mother, and the proposed daughter was not already assigned to a mother with higher confidence.

If a segmented budneck touched less than two cells (or more than two cells), up to two dilations (or erosions) were performed in an attempt to find exactly two cells that overlapped with the budneck. If this was successful, the pairing process was attempted for a second time. Otherwise, no pairing was proposed from the given budneck.

Two notable changes were made to the above algorithm when the first time point was being processed. First, proposed mothers were not required to be 1.5 times the size of the daughter; merely being larger than the daughter was sufficient. Second, proposed daughters were not required to have appeared after their proposed mother.

In some cases, the methods described above led to new cells that could not be identified as mothers or daughters. This was often caused by inadvertent oversegmentation of a hollow cell into several pieces when the watershed function was used to separate clumps of cells. It is common for a cell to appear hollow when it contains a large vacuole. To deal with this, all new nondaughter nonmother cells that were not present during the first time point were slightly dilated to include the cut lines used to separate them from their neighbors in the watershed step, effectively reassembling the oversegmented cell. All holes in the segmentation image were then filled before redoing the watershed step, and the cell/lineage tracking routines were repeated for a second and final time.

Postprocessing. Once cells and lineages had been tracked for all time points, the tracking data were inspected for errors and the following postprocessing steps were used to either correct the suspected errors or remove the affected cells from the analysis.

Removal of transient cells. Labels that were found in fewer than three time points and not in the final time point were likely a result of false positives in the segmentation or inaccurate cell tracking. These labels were removed from the data set.

Connection of cell trajectories. Errors in cell tracking sometimes caused a cell's label to change, incorrectly suggesting that one cell had disappeared and a different cell had appeared. The Hungarian algorithm was used to match disappeared labels with newly appeared labels to correct this mistake.

For each time point *t*, labels that were present in the previous time point *t*-1 but absent in all time points from *t* onward acted as agents in the assignment problem. Labels that were present in *t*, absent from all previous time points, and larger than half of the median cell size in *t* acted as tasks. This requirement on cell size ensured that the trajectories of small, newborn cells were not falsely connected to the trajectories of preexisting cells. It was also required that all agents and tasks have their centroids at least 50 pixels away from the edges of the image so that trajectories of labels that had recently entered or exited the field of view were not falsely connected. The cost Cij of assigning task j to agent i was taken to be Cij = Dij + 0.25(Sj/Si) where Dij was the Euclidean distance between the centroids of the two cells, Sj was this size of cell j, and Si was the size of cell i. The cost matrix C is then modified by giving infinite cost to the following elements: Elements with Dij > 50; elements with Sj/Si > 3; elements with Sj/Si < 0.66; elements for which i is "full grown" and Sj/Si > 1.25; and elements for which i is "full grown" and Sj/Si < 0.8. (A cell was considered to be "full-grown" if it was at least 25% larger than the median cell size.)

The assignment problem given by the resulting cost matrix was solved using the same version of the Hungarian algorithm as was used for cell tracking. For every matching pair of labels, i and j, all instances of label j in the data set were replaced by label i, thus connecting the two trajectories.

Removal of large newborn cells and their daughters. In cases where the segmentation algorithm was unable to resolve large clumps of cells, these clumps would appear as one large cell. Cells that, in their first appearance, were greater than 2 times the median cell size of that time point and whose centroids were not within 50 pixels of the image edges were suspected to be a result of incorrectly segmented clumps. These cells, along with all daughters that had been assigned to them, were removed from the data set.

Movie generation. A time-lapse movie in AVI format was created for each field of view to show the results of segmentation, cell tracking, lineage tracking, and postprocessing (Movie S1). Each time point of the movie consisted of the following components overlaid onto each other: An unfocused bright-field image to show cell borders (grayscale); boundaries of detected cells (blue); boundaries of detected cells that were removed during postprocessing (red); cell labels, displayed at the centroid of each detected cell (red); lines connecting the centroid of every cell to that of its mother (green); and a time stamp showing the time point of each frame (white).

Performance of the lineage-tracking algorithm. From each experiment we collected data for ~30,000 cells. To estimate how well the algorithm tracks every cell, we plotted distributions of cells based on the percentage of tracked time points out of the total tracking period (Fig. S5*A*). Over 80% of cells in the experiment were tracked for 90% of the time. To verify the accuracy of the image-analysis software we randomly picked cells from different chambers of the array and followed the performance of their segmentation, tracking, and lineage assignment in every time point of the experiment. Number of errors in segmentation and tracking did not exceed 2% of all assessed time points whereas lineage assignment failed in 16% of cases deteriorating with time (Fig. S5*B*, *Lower*). All cells were tracked accurately in every time point for the first 5 h, after which the performance started to slowly deteriorate with 70% percent of cells still tracked for 100% of time at the end of the experiment (Fig. S5*B*, *Upper*). The performance decay of the image-analysis software toward the end of experiments was mainly due to the high cell density in chambers, which caused distortion of the monolayers and increased moving distance of cells between individual time frames.

Fluorescence quantitation. CFP and mCherry fluorescence intensities were measured for every cell in every time point as the mean of the cell's pixel intensities (after flat-field correction). The background intensity of each image was also measured as the mean, median, and mode of all "background" pixels, where the background pixels were identified by thresholding the image using Otsu's method after normalizing the pixel intensities to [0,1].

Figure Generation. Single-cell data on mCherry, CFP, YFP, areas, and lineages were exported to Python software and custom-made scripts were used to generate figures and analyze data.

SI Results and Discussion

Hypotheses on the Mechanism of *ste50Δ* Asymmetry. Hydroxyurea treatment, which leads to cell synchronization in S phase and enlargement of buds, eliminated the response asymmetry and cell-cycle asymmetry between newborn daughters and mothers of *ste50Δ* strain. This result implies that the origins of the *ste50Δ* asymmetry are connected with the cell cycle. It has been proposed that the delayed G1 phase in daughters is maintained through daughter-specific factors Ace2 and Ash1 by repression of G1 cyclin *CLN3* (10, 11). Reduced Cln/CDK activity in young cells may lead to lower cell-cycle inhibition of the pheromone signaling, which happens through Cln/CDK disruption of the interaction between the scaffold protein Ste5 and plasma membrane (12). During pheromone signaling, Ste5 brings the first of the MAPK cascade proteins, Ste11, to the membrane where it is activated by Ste20 (13). The association of Ste11 and Ste20 is promoted by Ste50 (14). Although the absence of Ste50 causes a mating defect, it was shown that this phenotype can be rescued by overexpression of Ste11 (14, 15). Thus, it is possible that the reduced inhibition of signaling in new daughters creates higher concentration of signaling components that may allow some *ste50Δ* daughters to establish connection at the membrane and transmit the signal despite Ste50 absence. Here stochastic variations in signaling components may also play a role in determining which daughter cells can initiate signaling. In addition, it may be that the small size of daughter cells leads to an enhanced interaction of Ste5 with the membrane, partially abrogating the absence of Ste50.

An alternative explanation of *ste50Δ* asymmetry could lie in nonequal distribution of signaling components at division and there is considerable evidence for asymmetric segregation of molecules with a bias toward daughter cells. For example the protein Cdc42, which is positioned upstream of Ste50 in the membrane and is implicated in facilitating Ste20 phosphorylation (14, 16), has been shown to be asymmetrically segregated toward the shmoo tip and the bud site during division (17). Also, Geyer et al. reported that Cbk1, a protein kinase that controls daughter-specific production of several proteins, is functionally restricted to daughter cells and interacts with pheromone pathway proteins Ste5 and Ste50 (18–21). Clearly cell-cycle effects and asymmetric segregation of molecules are not necessarily independent processes. For instance, daughter-specific localization of transcription factors result in longer G1 phase in daughters compared with mothers as mentioned earlier (10, 11). In another example, Gehlen et al. showed that a delay in G2/M transition increased plasmid segregation into daughters at division, which would be otherwise restricted due to nucleus geometry (22).

1. Unger MA, Chou HP, Thorsen T, Scherer A, Quake SR (2000) Monolithic microfabricated valves and pumps by multilayer soft lithography. *Science* 288(5463):113–116.
2. Thorsen T, Maerkl SJ, Quake SR (2002) Microfluidic large-scale integration. *Science* 298(5593):580–584.
3. Falconnet D, et al. (2011) High-throughput tracking of single yeast cells in a microfluidic imaging matrix. *Lab Chip* 11(3):466–473.
4. Janke C, et al. (2004) A versatile toolbox for PCR-based tagging of yeast genes: new fluorescent proteins, more markers and promoter substitution cassettes. *Yeast* 21(11): 947–962.
5. Taylor RJ, et al. (2009) Dynamic analysis of MAPK signaling using a high-throughput microfluidic single-cell imaging platform. *Proc Natl Acad Sci USA* 106(10):3758–3763.
6. Sheff MA, Thorn KS (2004) Optimized cassettes for fluorescent protein tagging in Saccharomyces cerevisiae. *Yeast* 21(8):661–670.
7. Otsu N (1979) Threshold selection method from gray-level histograms. *IEEE Trans Syst Man Cybern* 9(1):62–66.
8. Kuhn HW (2005) The Hungarian method for the assignment problem. *Naval Res Logist* 52(1):7–21.
9. Ruusuvuori P, et al. (2010) Evaluation of methods for detection of fluorescence labeled subcellular objects in microscope images. *BMC Bioinformatics* 11:248.
10. Laabs TL, et al. (2003) ACE2 is required for daughter cell-specific G1 delay in Saccharomyces cerevisiae. *Proc Natl Acad Sci USA* 100(18):10275–10280.
11. Di Talia S, et al. (2009) Daughter-specific transcription factors regulate cell size control in budding yeast. *PLoS Biol* 7(10):e1000221.
12. Strickfaden SC, et al. (2007) A mechanism for cell-cycle regulation of MAP kinase signaling in a yeast differentiation pathway. *Cell* 128(3):519–531.
13. Bardwell L (2005) A walk-through of the yeast mating pheromone response pathway. *Peptides* 26(2):339–350.
14. Ramezani-Rad M (2003) The role of adaptor protein Ste50-dependent regulation of the MAPKKK Ste11 in multiple signalling pathways of yeast. *Curr Genet* 43(3): 161–170.
15. Ramezani Rad M, Jansen G, Bühring F, Hollenberg CP (1998) Ste50p is involved in regulating filamentous growth in the yeast Saccharomyces cerevisiae and associates with Ste11p. *Mol Gen Genet* 259(1):29–38.
16. Tatebayashi K, et al. (2006) Adaptor functions of Cdc42, Ste50, and Sho1 in the yeast osmoregulatory HOG MAPK pathway. *EMBO J* 25(13):3033–3044.
17. Slaughter BD, Smith SE, Li R (2009) Symmetry breaking in the life cycle of the budding yeast. *Cold Spring Harb Perspect Biol* 1(3):a003384.
18. Mazanka E, et al. (2008) The NDR/LATS family kinase Cbk1 directly controls transcriptional asymmetry. *PLoS Biol* 6(8):e203.
19. Colman-Lerner A, Chin TE, Brent R (2001) Yeast Cbk1 and Mob2 activate daughter-specific genetic programs to induce asymmetric cell fates. *Cell* 107(6):739–750.
20. Geyer CR, Colman-Lerner A, Brent R (1999) "Mutagenesis" by peptide aptamers identifies genetic network members and pathway connections. *Proc Natl Acad Sci USA* 96(15):8567–8572.
21. Weiss EL, et al. (2002) The Saccharomyces cerevisiae Mob2p-Cbk1p kinase complex promotes polarized growth and acts with the mitotic exit network to facilitate daughter cell-specific localization of Ace2p transcription factor. *J Cell Biol* 158(5): 885–900.
22. Gehlen LR, et al. (2011) Nuclear geometry and rapid mitosis ensure asymmetric episome segregation in yeast. *Curr Biol* 21(1):25–33.

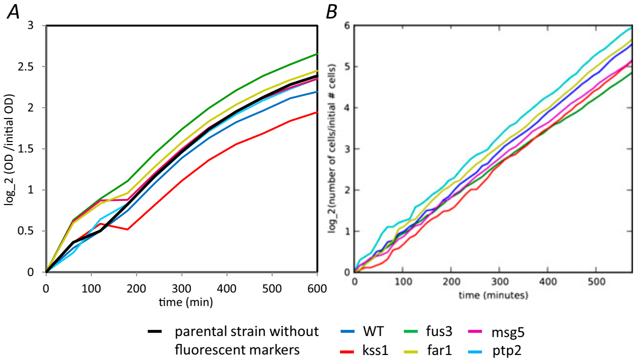

Fig. S1. Comparison of cell growth in a microwell plate and in a microfluidic device. Cells taken from exponential phase were grown at room temperature in synthetic glucose media (SCD) supplemented with 0.1% BSA. (*A*) Growth of parental strain BY4743 with no fluorescent markers (black) and knockout strains with three fluorescent markers in 96-well plate. Growth rate was measured as an increase in optical density at 600 nm using Tecan M200 Pro reader plate. (*B*) Growth of three-color strains in the microfluidic device.

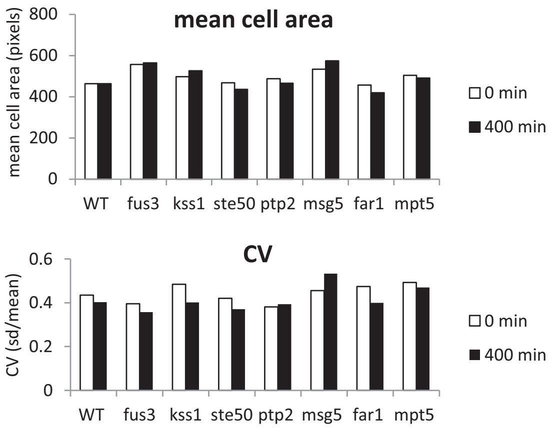

Fig. S2. Mean (*Upper*) and variability (*Lower*) of cell areas at the beginning of the experiment and after 400 min of growth in the microfluidic device for all eight strains.

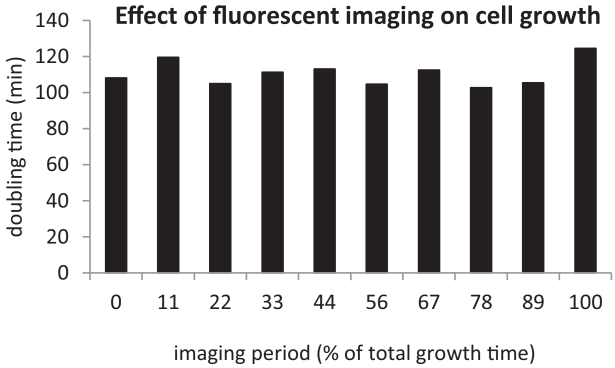

Fig. S3. Effect of fluorescent imaging on cell growth. WT cells were loaded in the chip and grown in SCD + 0.1% BSA. Each row of the device was periodically imaged in three fluorescent channels (YFP, CFP, mCherry) for different period from 0 min (0% of total imaging period) to 225 min (100% of total imaging period). Doubling time was calculated from the numbers of cells present at the beginning and at the end of the experiment.

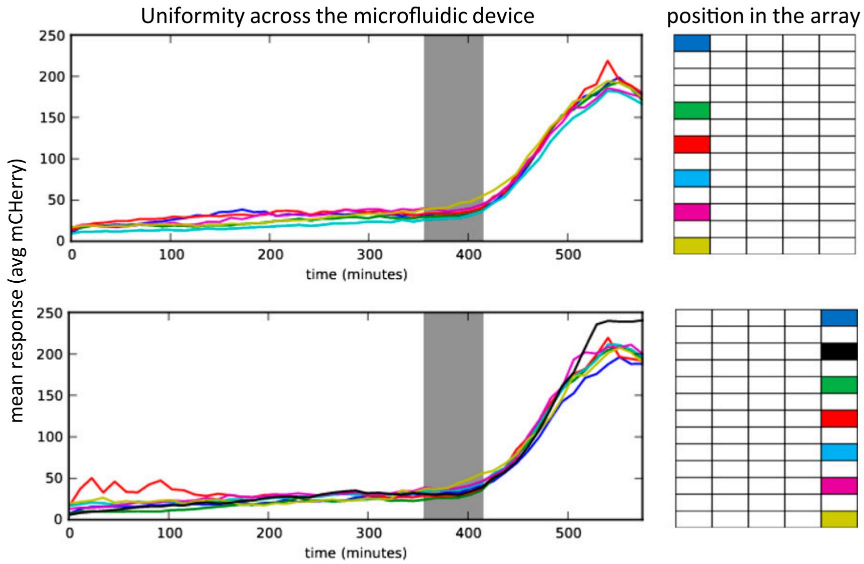

Fig. S4. Uniformity across the microfluidic device. WT cells were loaded in the first and fifth column of the device and every second row was exposed to 1 h of 100-nM α-factor. Automated imaging of the array was performed on 5 columns and 13 rows. Each line in the plot represents mean response of cells grown in individual chambers. Color of the line corresponds to color of the position in the array displayed on the left. Note that there were no cells in the third row of the first column, hence no data for that particular chamber.

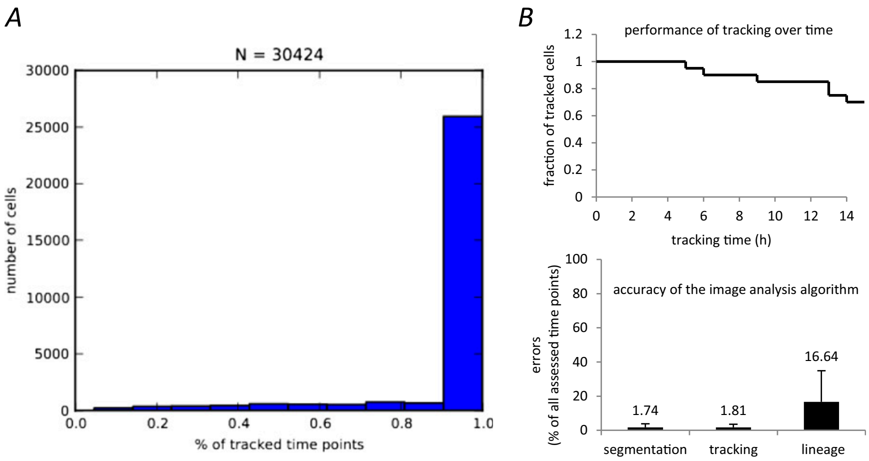

Fig. S5. Error statistics of image analysis algorithm. (*A*) Distribution of cells according to the number of tracked time points (percent of tracked time points out of the total tracking period); *n* = number of analyzed cells from one experiment. (*B*) Manual verification of image analysis software on 20 random cells in each time point of a 14-h-long experiment. *Upper* shows fraction of tracked cells over time. *Lower* shows number of errors in segmentation, tracking, and lineage assignment as a percentage of all assessed time points.

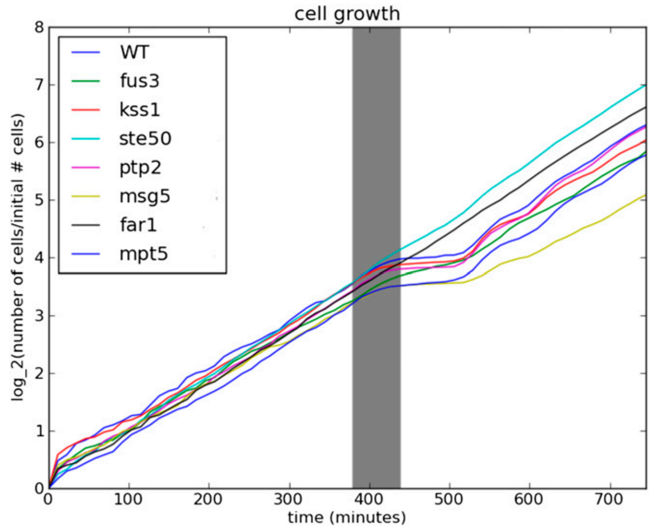

Fig. S6. Growth rate of all tested strains in SCD + 0.1% BSA with 1-h pulse of 100-nM α-factor (gray rectangle).

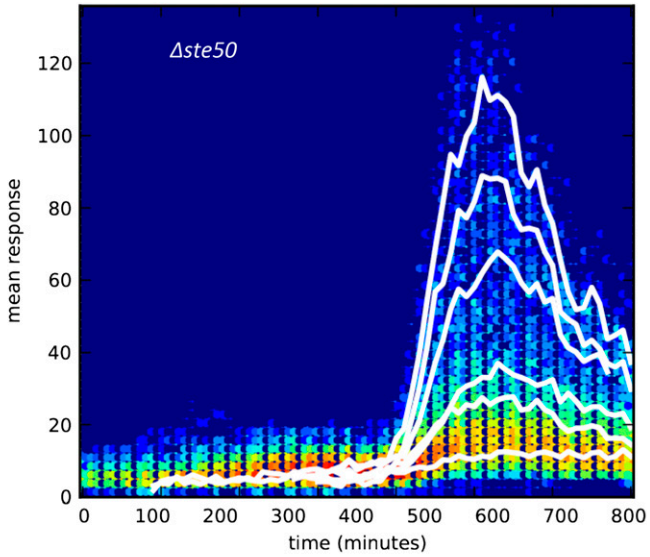

Fig. S7. High variability of *ste50Δ* arises from majority of nonresponding cells and a subpopulation of responding cells. A density plot of *ste50Δ* response over time with representative trajectories.

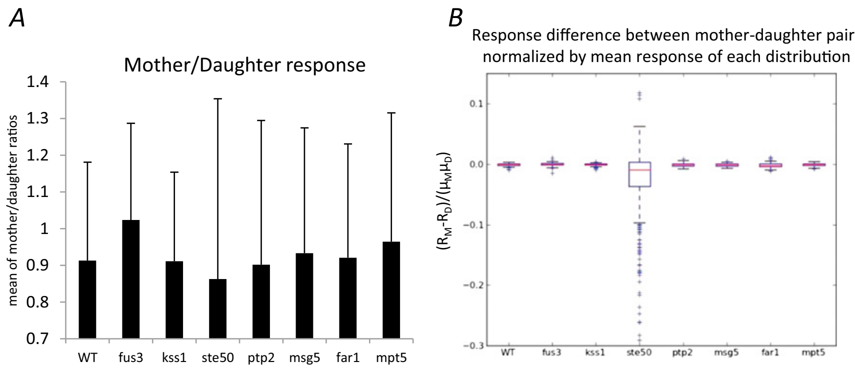

Fig. S8. Comparison of mother and daughter response in all tested strains. (*A*) Mean of the response ratios between mothers and daughters with SDs. Note that although *ste50Δ* strain has the lowest mother/daughter ratio, the difference is not as apparent as on the scatterplots in Fig. 2*C* due to a big population of *ste50Δ* cells that do not respond irrespective of their mother/daughter status. Averaging of single-cell data hides the asymmetric subpopulation. (*B*) Box plot of response difference between mother–daughter pairs (R_M–R_D) normalized by mean response of mothers (μ_M) and mean response of daughters (μ_D).

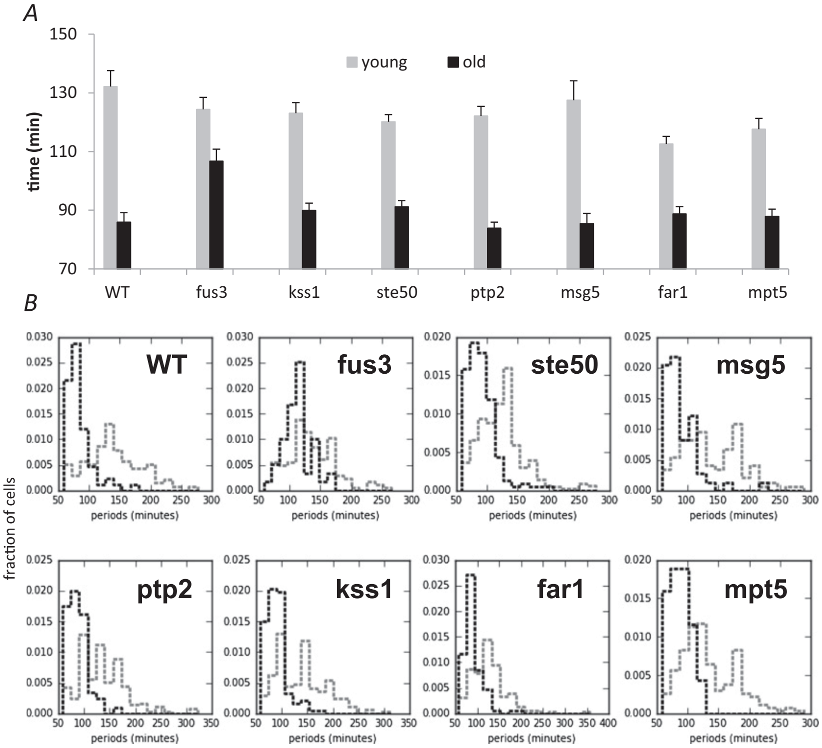

Fig. S9. Cell-cycle periods of young daughters (young—gray), described as cells that never divided before, and mothers (old—black) under normal growth conditions in SCD-0.1% BSA media. (*A*) Mean cell-cycle periods with SEs; (*B*) distribution of cell-cycle periods.

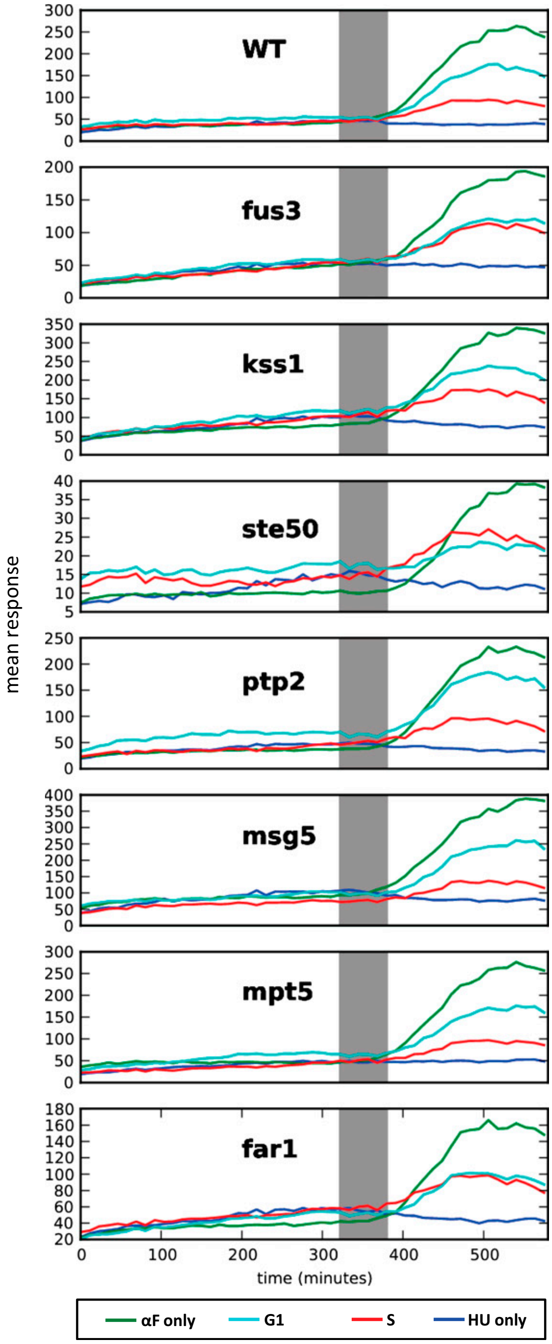

Fig. S10. Cell-cycle modulation of pheromone signaling in hydroxyurea (HU) synchronized cells of all strains. Nonsynchronized cells (α–F only), cells synchronized in G1 phase (G1), cells synchronized in S phase (S), and cells synchronized by HU but not exposed to pheromone (HU only). Gray area represents period of pheromone stimulation.

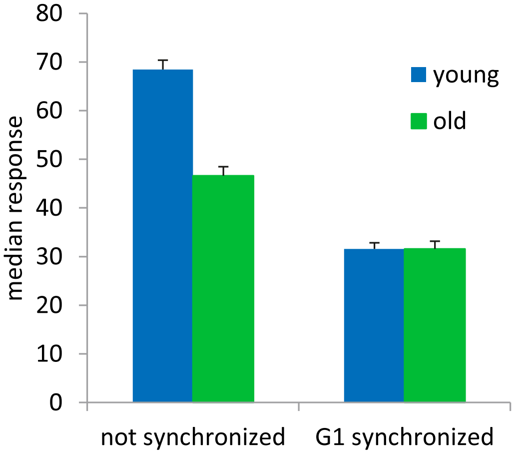

Fig. S11. HU synchronization abolishes the difference in *ste50Δ* pheromone response between young daughters (young) and mothers (old). Cells were either directly exposed to pheromone (not synchronized) or synchronized by HU in G1 phase and then exposed to pheromone (G1 synchronized). Error bars are SEs.

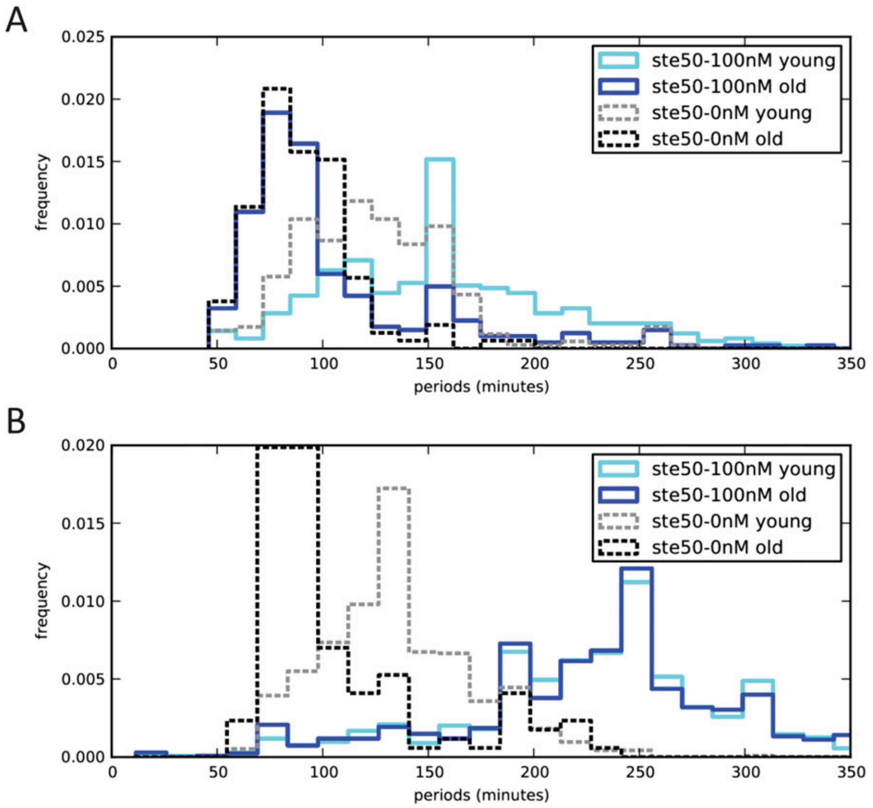

Fig. S12. HU synchronization abolishes the difference in pheromone-induced cell-cycle periods between young daughters (young) and mothers (old): (*A*) not synchronized, (*B*) synchronized in G1 phase. Cell-cycle periods before HU treatment were measured as a control (0 nM young and old). Only periods that started before the pheromone induction and ended after beginning of the induction were measured as pheromone-induced periods (100 nM young and old).

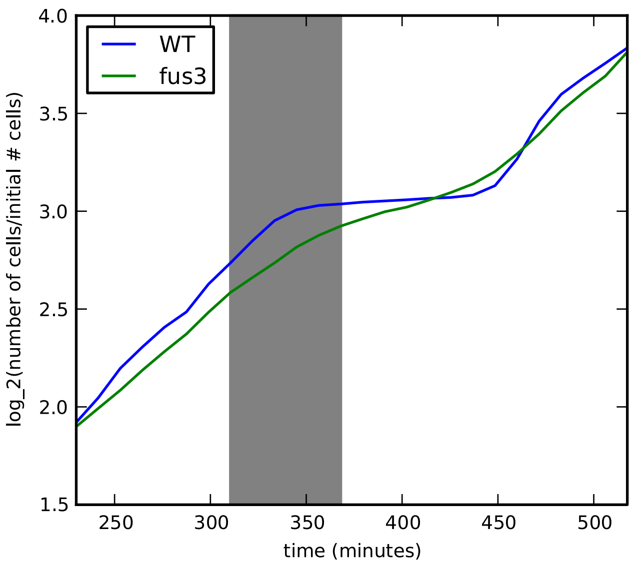

Fig. S13. Incomplete growth arrest of *fus3Δ* population upon pheromone stimulation compared with full arrest of WT. Gray area represents period of pheromone stimulation.

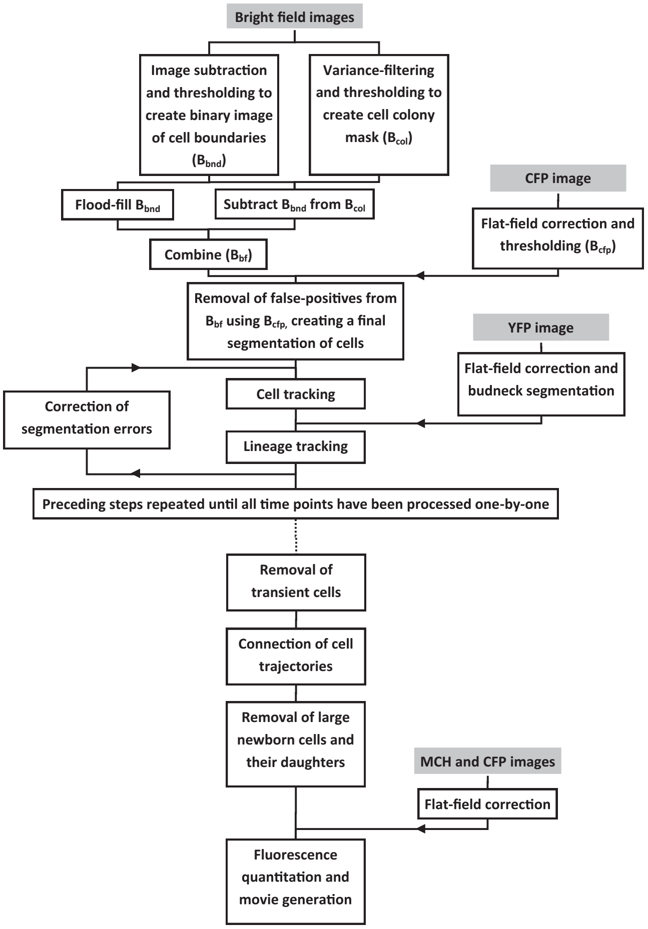

Fig. S14. Flowchart of the image-analysis pipeline describing segmentation, tracking, lineage assignment, and fluorescence quantitation of single cells.

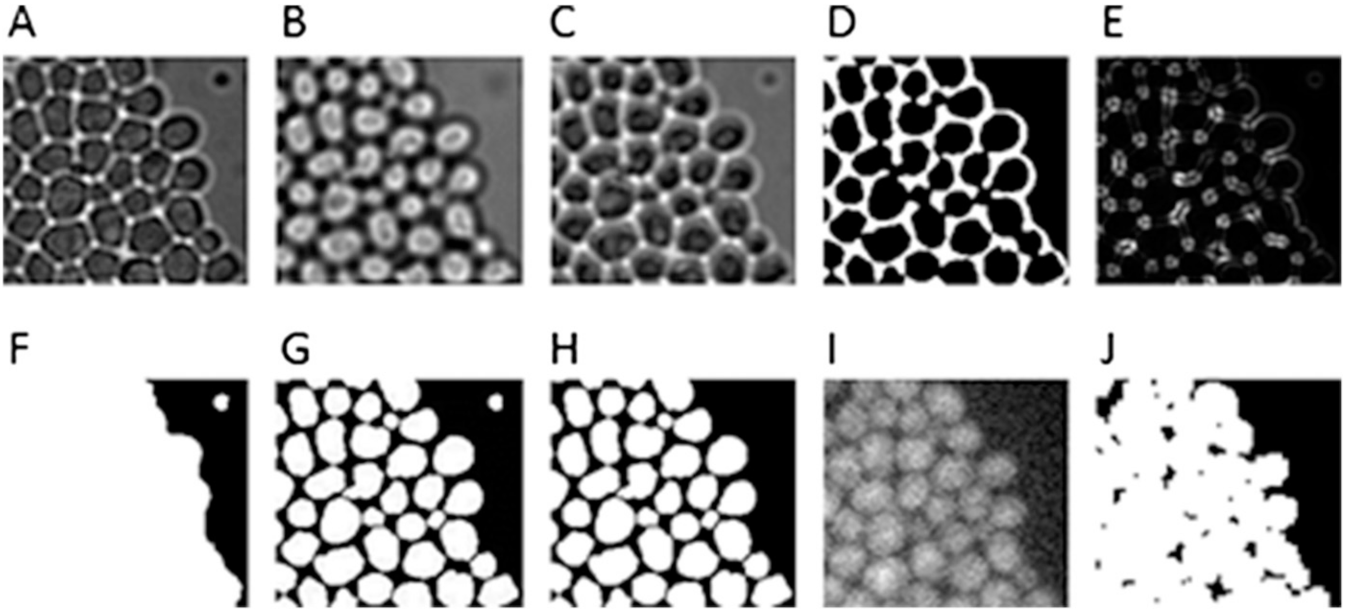

Fig. S15. Cell segmentation. (*A*) Unfocused bright-field image (cells are 3.5 μm above focal plane) after normalization. (*B*) Unfocused bright-field image (cells are 3.5 μm below focal plane) after normalization. (*C*) Difference of *A* and *B* after normalization. (*D*) Cell boundaries (B_{bnd}), the result of thresholding *C*, removing small objects, and closing. (*E*) The result of variance-filtering *A*. (*F*) Cell-colony mask (B_{col}), the result of thresholding *E*, dilating, filling holes, and eroding. (*G*) The final segmentation image before using CFP information for false-positive removal (B_{bf}). (*H*) The final segmentation image after using CFP for false-positive removal. (*I*) The raw CFP image, after normalization. (*J*) Segmented CFP image (B_{cfp}), the result of thresholding and opening *I*.

Table S1. Details of the strains used in this study

Strain name	Genotype
WT(737D)	*MATa met15Δ 0 ura3Δ 0 leu2Δ 0::*CDC10-YFP-LEU2 *bar1Δ*::HphNT2 *his3*::PRE-mCherry-HIS3 *ho::*ACT1pr-yECFP-CaURA3
far1Δ	*MATa met15Δ 0 ura3Δ 0 leu2Δ 0::*CDC10-YFP-LEU2 *bar1Δ*::HphNT2 *his3*::PRE-mCherry-HIS3 *ho::*ACT1pr-yECFP-CaURA3 *far1Δ*::KanMX4
fus3Δ	*MATa met15Δ 0 ura3Δ 0 leu2Δ 0::*CDC10-YFP-LEU2 *bar1Δ*::HphNT2 *his3*::PRE-mCherry-HIS3 *ho::*ACT1pr-yECFP-CaURA3 *fus3Δ*::KanMX4
kss1Δ	*MATa met15Δ 0 ura3Δ 0 leu2Δ 0::*CDC10-YFP-LEU2 *bar1Δ*::HphNT2 *his3*::PRE-mCherry-HIS3 *ho::*ACT1pr-yECFP-CaURA3 *kss1Δ*::KanMX4
msg5Δ	*MATa met15Δ 0 ura3Δ 0 leu2Δ 0::*CDC10-YFP-LEU2 *bar1Δ*::HphNT2 *his3*::PRE-mCherry-HIS3 *ho::*ACT1pr-yECFP-CaURA3 *msg5Δ*::KanMX4
ptp2Δ	*MATa met15Δ 0 ura3Δ 0 leu2Δ 0::*CDC10-YFP-LEU2 *bar1Δ*::HphNT2 *his3*::PRE-mCherry-HIS3 *ho::*ACT1pr-yECFP-CaURA3 *ptp2Δ*::KanMX4
ste50Δ	*MATa met15Δ 0 ura3Δ 0 leu2Δ 0::*CDC10-YFP-LEU2 *bar1Δ*::HphNT2 *his3*::PRE-mCherry-HIS3 *ho::*ACT1pr-yECFP-CaURA3 *ste50Δ*::KanMX4
mpt5Δ	*MATa met15Δ 0 ura3Δ 0 leu2Δ 0::*CDC10-YFP-LEU2 *bar1Δ*::HphNT2 *his3*::PRE-mCherry-HIS3 *ho::*ACT1pr-yECFP-CaURA3 *mpt5Δ*::KanMX4

All strains are *MATa* type in S288C background. They contain a mating specific reporter (PRE-mCherry), a budneck marker (CDC10-YFP), a whole-cell fluorescence marker (ACT1pr-yECFP), and are deleted for *BAR1* gene. In addition, seven strains are deleted for components of the pheromone signaling pathway.

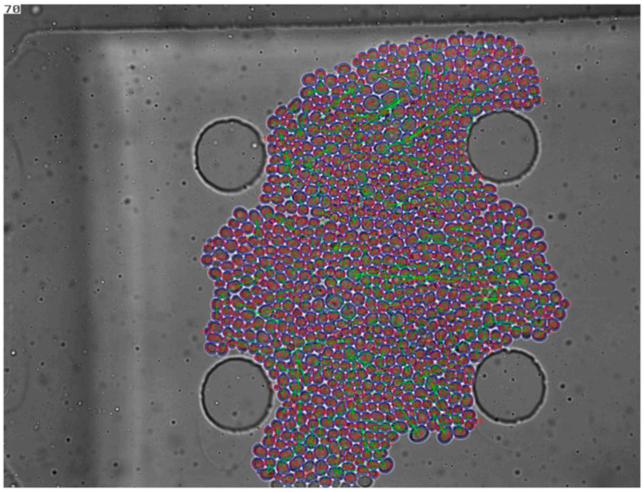

Movie S1. Lineage tracking analysis of *far1Δ* growth in the left part of a microfluidic chamber during 14-h-long experiment.

Movie S1